Materials and Design 203 (2021) 109575

Contents lists available at ScienceDirect

Materials and Design

journal homepage: www.elsevier.com/locate/matdes

Tailoring cold spray additive manufacturing of steel 316 L for static and cyclic load-bearing applications

Sara Bagherifard [a,*], Jan Kondas [a,b], Stefano Monti [a], Jan Cizek [c], Fabrizio Perego [a], Ondrej Kovarik [d], Frantisek Lukac [c], Frank Gaertner [e], Mario Guagliano [a]

[a] *Department of Mechanical Engineering, Politecnico di Milano, Milan, Italy*
[b] *Impact Innovations GmbH, Bürgermeister-Steinberger-Ring 1, 84431, Haun/Rattenkirchen, Germany*
[c] *Institute of Plasma Physics of the Czech Academy of Sciences, Prague, Czech Republic*
[d] *Faculty on Nuclear Sciences and Physical Engineering, Czech Technical University, Prague, Czech Republic*
[e] *Helmut Schmidt University - University of the Federal Armed Forces Hamburg, Hamburg, Germany*

HIGHLIGHTS

- CSAM parts exhibited <1% porosity and strengths similar to bulk material.
- As-sprayed and heat treated samples showed fatigue strength comparable to cast material.
- As-sprayed samples exhibited anisotropic crack growth behavior.
- Heat treated samples showed identical crack growth rates to the cold rolled sheets.
- Cold spray showed significant potential for AM of structural components.

GRAPHICAL ABSTRACT

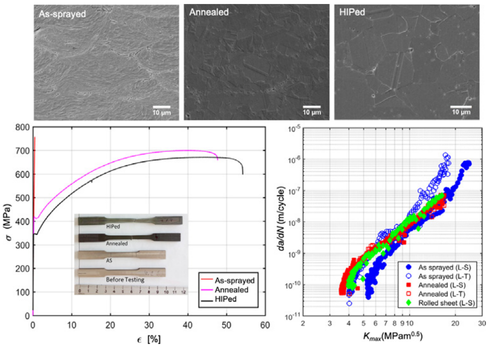

ARTICLE INFO

Article history:
Received 29 October 2020
Received in revised form 8 January 2021
Accepted 7 February 2021
Available online 13 February 2021

Keywords:
Kinetic deposition
3D-printing
Freestanding
Fatigue
Crack propagation

ABSTRACT

Thanks to the low working temperature, less product size limitations and one order of magnitude higher deposition rates compared to the established additive manufacturing techniques, more attention has been brought to the potential of cold spraying for additive manufacturing . As a process dealing with deformation of solid particles possibly leaving non-bonded interfaces and causing work hardening, any optimization should (i) adjust spray parameters to obtain high performance as-sprayed parts and (ii) tune ductility and internal stresses by post-treatments. The present study first deals with strategies to optimize spray parameters for fabrication of high performance steel 316 L deposits. Next, the performances of deposits are further adjusted by various heat treatments. The structural strength of the freestanding samples before and after the heat treatments is evaluated under static and cyclic axial loading and supported by fatigue crack growth rate analysis. The results highlight the feasibility of obtaining high quality steel 316 L deposits using N_2 as process gas, rather than the costly He that is commonly suggested. This study demonstrates the potential of cold spraying to be used for deposition of freeform structural components with a static strength comparable to that of bulk and laser-based additive manufactured materials and a fatigue strength similar to that of bulk cast material.

1. Introduction

Cold spraying (CS) is an emerging deposition technique mostly used for mass production of high electrical and thermal conductive layers,

---

* Corresponding author.
E-mail address: sara.bagherifard@polimi.it (S. Bagherifard).

https://doi.org/10.1016/j.matdes.2021.109575

Nomenclature

a_0	Initial crack length
da/dN	Crack propagation rate
ΔK_{eff}	Effective stress intensity factor range
η	Impact to critical velocity ratio
K_{max}	Maximum stress intensity factor
p_{gas}	Gas pressure
R	Stress ratio
T_{gas}	Gas temperature
T_m	Particle melting temperature
T_p	Particle impact temperature
v_{crit}	Critical velocity
v_p	Particle impact velocity
AM	Additive manufacturing
CDD	Coherently diffracting domains
CS	Cold spray
DD	Ductile dimples
EDM	Wire-electro discharge machining
HIP	Hot isostatic pressing
IP	Inter-particle decohesion
LPBF	laser powder bed fusion
OM	Optical microscopy
PSD	Particle size distribution
SEM	Scanning electron microscopy
SENB	Single edge notched sample
SF	Striation fields
TG	Trans-granular
UTS	Ultimate tensile strength
XRD	X-ray diffraction

corrosion resistant coatings, dimensional restoration and spot repair [1–4]. Based on experimental investigations, efficient bonding is attained upon impact at a velocity superior to a critical value [5] that depends on the thermo-mechanical properties of the spray material [6]. The low working temperature minimizes tensile thermal stresses, oxidation, and grain growth; besides, the outstandingly high deposition rate and, as no controlled atmosphere chambers are needed, less limitations on the deposit dimensions, have lately brought significant attention to the application of CS for additive manufacturing (AM) [7–10]. The main shortcomings of CS as compared to common AM technologies concern the lower resolution and geometrical precision. A detailed comparison between CS and laser-based AM technologies is elaborated elsewhere [11].

Material strength, in particular under cyclic loading, is a crucial property to be considered in promoting the use of CS for AM. Sufficient structural integrity under cyclic loading can pave the way for CS to be recognized by the ASTM and ISO International societies as an AM technology. Any deposit development in CS for AM has to address combined points of (i) deposit optimization with respect to intrinsic properties such as strength or conductivity, and (ii) application of post treatments to further adjust the deposit properties. During CS deposition, voids can form due to inadequate kinetic energy, too low particle temperature to enforce thermal softening, surface imperfections or inadequate packing of powder particles [6]. Even at low or zero porosity, there could be some non-bonded interfaces acting as planar 2D defects that could restrict the deposit strength. The presence of the imperfections can be effectively diminished by post heat treatments, which, aside from closing the non-bonded interfaces by surface diffusion along the planar defects, could further bring the benefit of restoring the deposit ductility through recrystallization. Nevertheless, to maintain the post-deposition annealing treatment technically realistic (considering the time scales and the temperatures needed for the diffusion), the quantity and size of the initial defects and porosity should be minimized by a thorough optimization of deposition parameters. For meeting thresholds of needed initial deposit properties, only data on strength or electrical conductivity in comparison to bulk material can provide sufficiently exact information. Correlation of in-plane electrical conductivity and tensile strength has been used in the past to provide an insight towards the presence and density of non-bonded interfaces, microstructural defects, and pores [12,13].

To make the process cost-competitive, the spray conditions should be tuned for N_2 (less costly compared to He) as process gas; at the same time, the post treatments must be also selected under economic considerations. The strategy for developing CS as a competitive AM technique separately addresses optimization of deposition parameters and investigates the effects of post treatments to provide a comprehensive understanding. Due to high deposition rates and large deposition size, CS can operate at significantly competitive costs, if N_2 can be used as process gas. According to detailed internal cost calculations supplied by Impact Innovations, the CS deposit serial production cost for 316 L was estimated to be 40 €/kg, 57% of which counts for the powder. Performing a detailed comparison between CS and other commonly used AM technologies is not the main focal point of this study. However, based on the provided cost estimate, it is safe to state that the CS technology possesses a notable economic advantage when compared to the laser-based AM technologies, especially for the production of medium/large size parts without intricate geometries [14,15].

Herein, we focus on 316 L stainless steel as an attractive option for biomedical, petrochemical, marine and architectural applications thanks to biocompatibility, high corrosion and high temperature oxidation resistance. 316 L has been deposited by CS in the past on multiple metallic substrates, using a variety of particle size distributions (PSD) [16], different crystallite sizes and phase contents [17] or multi-material powders [18,19] to enhance the density of the coating, as well as corrosion and wear resistance. Substrate pre-heating was used to enhance the quality of 316 L coatings; the results indicated enhanced adhesion strength but no significant effect on the coating porosity [20]. Multiple studies have been performed to analyze the effect of process parameters and particle morphology on the properties of cold spray 316 L deposits [21–23]. These studies have shown that bulk material properties cannot be easily achieved for 316 L CS deposits using N_2 as process gas [24], leading to the conclusion that dense 316 L deposits of high quality can only be attained by utilizing He [25]. One of the highlights of the present work is demonstrating that an equally good or better performance can be reached by using N_2. In the literature, also laser post re-melting was adopted to decrease the 3–8% porosity of 316 L deposits to <1%, but without reporting consequences for deposit tensile strength [26]. To develop an industrially sustainable process, herein, we successfully demonstrate the possibility to optimize the spraying parameters for obtaining high performance deposits by using N_2 and commercially established annealing techniques.

Regarding process parameter optimization, the main influences on the deposit quality are given by the CS gas pressure and temperature [27,28]. For alloys that show thermal softening, the deposit quality can be estimated by a quality parameter $\eta = v_p(T_p)/v_{crit}(T_p)$ as the ratio between particle impact velocity v_p and critical velocity v_{crit} for bonding at attained particle impact temperature T_p [29]. The η-parameter is considered to supply an all-inclusive dimensionless description for CS deposition to consider contributions of material properties and impact conditions of different particle sizes under various process parameters. It is correlated with the cohesive strength of the CS deposits, as long as the temperature is far from the melting temperature of the powders [4]. The key issue for deposit optimization is to find the right match of powder size and spray parameter sets. Respective concepts are incorporated in a commercial software [30]; however, the practical realization of high-end parameter sets is often challenging and limited by the input data. In a first approach, usually bulk material data is taken as input. More reliable input can be gained by experimentally measuring the powder strength for considering possible effects by the powder production process or oxygen contents [31,32]. Reaching or exceeding thresholds of coating quality in the as-sprayed state are the prerequisite for the success after post-processing.

The second stage of this study deals with the other typical concern for CS deposits, the limited ductility caused by the notable work hardening of the deformed particles (splats) and possibly remaining non-bonded interfaces acting as crack nuclei [33,34]. To address this drawback, annealing has been widely used for 316 L CS coatings, reporting enhanced bonding between the particles and improved ductility by uniform recrystallization at temperatures >1000 °C [25,35–37]. In the present study, in addition to annealing, hot isostatic pressing (HIP) is also considered as a high-end technology commonly used to uphold powder consolidation and porosity reduction in cast parts. This process involves applications of high isostatic pressure at high temperatures (generally higher than $0.7T_m$) to reduce, if not eliminate, internal porosity. The application of HIP to CS 316 L deposits was recently reported to considerably improve deposit density and enhance tensile strength and ductility [38]. Comparison of both post treatments would allow for identifying the more suitable and possibly more economical heat treatment.

Studying the crack growth behavior is also necessary for evaluating the functionality of AM materials [39]. Despite the importance of the subject, there is a considerably limited number of studies in the literature on fatigue strength and crack growth behavior of freestanding CS deposits and [40], demonstrating that CS application for AM is still under development. One study on fatigue strength of CS 316 L deposit after 1 h annealing at 1100 °C, reported lower axial fatigue strength as compared to conventionally prepared 316 L samples. Weak interparticle bonding and presence of pores were mentioned as the primary sources of crack initiation [41]. On the general topic of fatigue crack growth in CS deposits, Gavras et al. performed a series of systematic studies on the effect of post heat treatments on small and large crack propagation rates in Al6061 alloy deposits [42,43]. In these studies the differences between crack initiation threshold values for the rolled bulk material and the CS deposits were justified mainly by the role of grain size in different series [42,43]. Freestanding deposits of cold sprayed pure metals including Cu, Al, Ni, and Ti represented significantly lower fracture toughness as compared to their bulk material counterparts [44].

Considering the limited data available on structural integrity of freestanding CS deposit and the importance of the topic in promoting the recognition of CS as an AM technology, this work aims to provide a systematic study on static strength, fatigue endurance and fatigue crack propagation behavior of bulk 316 L parts. Herein, the strategy to develop high performance steel 316 L bulk parts by CS is described in two major sections. Part one deals with CS parameter optimization for best deposit qualities in as-sprayed state at reduced costs by employing N_2 as process gas. The optimization process is supported by analyzing the correlation between impact condition and the resulting tensile strength and electrical conductivity. Part two contains detailed experiments concerning the influence of post heat treatments to further improve the properties of optimum deposits with respect to microstructure, porosity, microhardness, phase content, residual stresses and microstrain. Major focus is then given on mechanical properties of the deposits including tensile static and axial fatigue strength as well as crack propagation behavior. The results reveal the high potential of CS to obtain 316 L deposit with characteristics comparable to those reported for laser-based AM and bulk cast/forged materials.

2. Materials and methods

2.1. Feedstock powder

Commercially available gas atomized 316 L stainless steel powder (Sandvik Osprey LTD) with two different particle size distributions (PSD) were used to find the most promising spray parameters. Particle size analysis was performed using Mastersizer2000 instrument (Malvern PANalytical Ltd., UK). The analyses reveal particle size of d10 = 12 μm, d50 = 18 μm, d90 = 29 μm for the fine, and d10 = 19 μm, d50 = 29 μm, d90 = 44 μm for the coarse powders. Fig. 1 shows the powder particles that illustrate a predominantly spherical shape with rather smooth surface morphology. The inserts in Fig. 1 show the microstructures of single powder particles, that turn out to be defect free, exhibiting equiaxed grains as obtained by rapid undercooling during powder atomization [45].

2.2. Selection of deposition parameters

The choice of parameters, as given in Table 1, was assisted by using the commercial software package from Kinetic Spray Solutions (KSS, Germany) [30]. Based on isentropic computational fluid dynamic (CFD) simulations of the two-phase flow through the nozzle and the free jet, the software calculates the particle impact conditions with respect to temperature and velocity for a range of particle sizes. Details on the CFD-calculation procedures are given in literature [28,29]. According to the KSS manual and the reference to the previous work, parameters of the CFD calculations are calibrated with respect to experimentally determined particle velocities for varied cold spray conditions using particle image velocimetry, as well as more detailed calculations by full 2D and 3D-CFD modelling using Ansys-Fluent software (ANSYS, Inc., Canonsburg, USA). As stated in [28,29], the respective calculations over-estimate the measured particle velocities by less than 5–10%. With respect to velocity analyses, it might be noted here that all optical methods such as particle image velocimetry as well as laser Doppler anemometry by higher intensity preferably provide data for larger particles of a given size distribution. Thus, considering all given uncertainties, the calibrated, isentropic calculations can be considered as a rather good estimate of individual particle velocities.

In addition, the KSS software calculates the critical velocities that need to be exceeded for bonding, and thus provides an estimation of the deposit quality parameter η. Details of respective procedures are given in literature [28,29]. Such pre-investigations were needed to explore whether suitable deposit qualities can be established by using N_2 as process gas within the available parameter range. As input data for the spray material, properties of soft annealed steel 316 L were taken from the KSS database. Such common reference for the two different powders would not count for individual impurity contents or microstructures.

Key spray parameters as process gas temperature, gas pressure, as well as powder size range, were varied for deposition by using an Impact Innovations ISS 5/11 CS system (Impact Innovations Inc., Germany). A convergent-divergent (de-Laval) SiC-Out1 (Impact Innovation GmbH) nozzle of 160 mm length with an expansion ratio of 5.6 was used in the experiments. The stand-off distance was set to 30 mm. The gun travel speed was kept at 500 mm/s. In all experiments, powder was injected 65 mm up-stream the nozzle throat.

2.3. Electrical conductivity

Electrical conductivity is considered as an index of a deposit quality; it mainly depends on the extent of bonded interfaces, besides other defect and impurity densities [46,47]. For CS deposits, electrical conductivity usually scales with tensile strength [12]. Thus, with respective calibration, this inexpensive and easy to perform method can be used for non-destructive testing in serial production. In the present study, electrical conductivity is paired with the tensile tests to develop individual correlations for the deposit properties. The in-plane conductivity of the deposits was assessed according to DIN EN16813 by applying a non-destructive eddy current method using a SigmaScope SMP10 (Helmut Fischer GmbH, Germany) at a frequency of 1250 kHz. The surfaces were ground and polished to avoid any influence from surface topography. The sensor head investigated a circular surface of 13 mm in diameter. Due to the low conductivity of the 316 L steel, it is expected that the

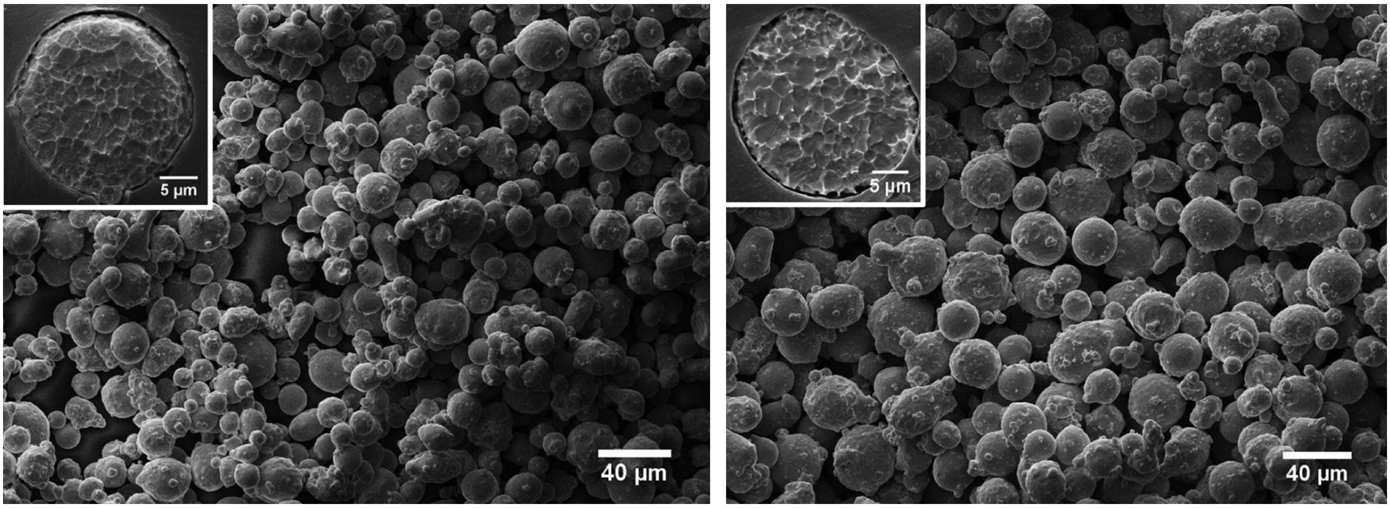

Fig. 1. SEM micrograph of 316 L feedstock powders; the inserts show etched cross sections of single powder particles (a) PSD 10–32 μm (b) PSD 15–38 μm.

eddy currents spread into a depth of about 500–700 μm at the selected frequency. Thus, the in-plane conductivity is averaged over about 3 to 5 spray layers and covers a deposit volume of around 70 to 90 mm^3. With a deposit thickness of >3 mm, any influence from the substrate material should be avoided. As a reference, also conductivities of the steel 316 L sheets were measured.

2.4. Heat treatments

Annealing was performed in air for 1 h at 1000 °C by using a heating rate of 30 °C/min in a Carbolite furnace (Carbolite Gero, Italy), followed by furnace cooling. The annealing parameters were selected based on their effect on promoting interparticle bonding and ductility [25,37,38]. HIP treatment was conducted using an EPSI HIP unit (EPSI NV, Belgium) at a temperature of 1100 °C with pressure of 100 MPa for 3 h by using heating and cooling rates of 10 °C/min in argon atmosphere. Due to the lack of data available for HIP treatment on 316 L CS deposits, the HIP parameters were selected based on the data available for standard cast bulk material. A more recent study published on the application of HIP on CS 316 L deposits used a temperature of 1000 °C with pressures of 0.1 MPa (for the first 4 h) and 150 MPa (next 4 h) [38].

2.5. Static tensile tests

During parameter optimization, 3 sub-size dog bone flat tensile samples (50 mm long) were extracted from 5 mm-thick depositions by wire-electro discharge machining (EDM) and milled to final shape with a thickness of 3 mm. The effect of spray gun travel direction was also evaluated by extracting samples parallel (L: longitudinal) and perpendicular (T: transversal) to the spray nozzle movement direction.

For optimized parameters, tensile tests were conducted on as-sprayed, annealed and HIPed samples by using 3 dog bone samples 100 mm long and 3 mm thick per each series. The tests were carried out following the ISO 6892-1 standard using an MTS Alliance RT/100 machine at a constant strain rate of 1 mm/min. The strains were calculated based on the data extracted from an extensometer attached to the samples during the tests. To exclude possible dimensional effects, the obtained results were then compared to those of the 50 mm long samples used for optimizing the process parameters (Fig. S1).

2.6. Microstructural characterization

Sample's cross sections were hot mounted in resin, mechanically ground with graded SiC papers, polished using diamond pastes down to 1 μm in abrasive size and chemically etched using Aqua Regia etchant. The etched cross sections were examined in bright field mode using a Leitz Aristomet optical microscope (OM) (Leitz Srl., Italy). A Zeiss EVO50 scanning electron microscopy (SEM) (Carl Zeiss Microscopy GmbH, Germany) was employed for revealing more details. The splat flattening ratio was extracted from the microstructural analysis as an index of the severity of plastic deformation upon impact. This parameter was defined as the ratio between the Feret diameter of single particles before and after deformation. Due to the complex in-flight dynamics during deposition, it is not feasible to track single particles before and after deposition. However, it is a common practice to compare the original particle size distribution with the average dimensions of multiple deposited splats. Although this method does not provide the possibility to perform a direct comparison; however, our past results and also the data available in the literature on different materials confirm the validity of this approach in providing an index of deformation extent upon deposition [10,48]. Splat dimensions were measured at different areas of the as-sprayed samples and analyzed to obtain the flattening ratio using ImageJ software [49].

Table 1
CS parameters, particle impact conditions, electrical conductivity, and tensile strength of the as-sprayed samples.

Sample series	Powder type	p_{gas} (MPa)	T_{gas} (°C)	v_p (m/s)	T_p (°C)	η	Conductivity (MS/m)	UTS (MPa)
A	Coarse	5	1000	690	688	1.51	1.185 ± 0.004	608 ± 7.9
B		5	1100	709	764	1.65	1.213 ± 0.003	765 ± 38.5
C		6	1000	706	682	1.54	1.205 ± 0.003	624 ± 85.7
D	Fine	5	1000	742	563	1.39	1.203 ± 0.002	591 ± 20.7
E		5	1100	767	632	1.51	1.222 ± 0.001	742 ± 17.7
F		6	1000	749	555	1.40	1.215 ± 0.003	595 ± 4.7

2.7. Porosity measurements

Two different approaches were considered for these tests including: (i) volumetric measurement by using the Archimedes buoyancy principle, and (ii) cross sectional image analyses of backscatter SEM observations. The volumetric measurements were conducted on four samples per series using a Precisa 100A–300 M electronic balance (Precisa Gravimetrics AG, Switzerland). This density kit evaluated the closed porosity of the material from the difference of samples' weight in air and distilled water. As a reference, a density of 7.9 g/cm^3 was considered for bulk 316 L [50]. 2D cross sectional image analysis was performed on eight SEM images from various areas of each sample's cross section.

2.8. Microhardness measurements

A Leica VMHT30A Vickers microhardness tester (M/S Leica, Germany) was used to conduct the measurements using a load of 100 gf and dwell time of 15 s on several positions across the samples' cross sections to inspect possible microhardness variations between the core and the surface. The reported data were averages of nine measurements.

2.9. Crystallographic phase and microstrain analyses

Prior to the measurements, the sample surfaces were mechanically polished down to 1-μm diamond paste to remove possible oxides and loosely bonded particles from the top layer. X-ray diffraction (XRD) phase analysis was then carried out using a D8 Discover vertical powder θ-θ diffractometer (Bruker AXS, Germany) with CoKα radiation ($\lambda = 1.78897$ Å) and a FeKβ filter. Bragg-Brentano geometry was employed with a 0.4° fixed divergent slit in the primary beam. The diffracted beam was detected by a 1D detector of type LynxEye. The 2θ angle ranged from 20° to 130°, with a step size of 0.03° and the total time of each step of 192 s.

Phase identification was performed by using Diffrac.Eva and X'Pert HighScore programs, both accessing the PDF-2 crystalline phases database from ICDD (International center for diffraction data). Quantitative Rietveld refinement was performed by TOPAS V5 software, where the size of coherently diffracting domains (CDD, crystallite sizes) and microstrains were determined from the width of Lorentzian and Gaussian components of the pseudo-Voigt profile functions, respectively [51,52]. Standard calibration samples were used for calculation of the profile broadening due to instrumental effects [53]. A preferred orientation (texture) correction according to the March-Dollase approach [54] was included to improve the intensities of the reflections.

2.10. Axial fatigue strength test and fractography analysis

Force-controlled constant amplitude axial fatigue tests with a stress ratio of $R = 0.1$ were conducted at room temperature following the procedure described in ASTM E466–15 using a Universal MTS test system (MTS, US) at a frequency of 30 Hz on as-sprayed, annealed and HIP treated series. The up and down staircase method presented by Dixon and Massey [55] was used to perform the tests considering a step size of 20 MPa. A statistical analysis approach according to ISO 12107 was used to analyze the fatigue test data and to calculate the fatigue strength corresponding to 2 million cycles. Fractographic analysis was performed on the fracture surfaces using Zeiss-Evo 50 SEM microscope.

2.11. Fatigue crack growth rate tests

Fatigue crack growth rates were measured in resonance bending on sub-sized ($4 \times 3 \times 32$ mm^3) single edge notched samples (SENB type according to ISO 12108 standard) with the notch depth of a_0 ~ 0.5 mm. Such bending sub-sized specimens are gaining popularity due to easy manufacturing, low amount of material required and an easy adaptation for combined loading [56]. The tests were performed on as-sprayed and annealed samples in two crack growth directions, parallel and perpendicular to the respective spray lines during deposition. Samples taken from annealed cold rolled sheets of 316 L (Matezex, Czech Republic) were used as reference. The samples were tested in resonance bending configuration shown in Fig. 2. The system consisted of two stiff yokes attached to the compliant sample forming a rotated H-shaped assembly suspended by a system of nylon strings. The first bending mode of the assembly was excited electromagnetically using air core coils acting on neodymium magnets located at the ends of the yokes (Fig. 2). The tests were performed in a rate-controlled mode [57]. In this mode, the exponential relation of the crack growth rate to the crack length $da/dN(a)$ is prescribed and the loading is adjusted accordingly. The resulting loading resembles the *K-control* mode recommended by ASTM 647, but brings several advantages, such as the explicit knowledge of the experiment duration and no risk of crack arrest. The samples were fatigue pre-cracked to $a = 1.1$ mm at a crack growth rate decreasing from 1×10^{-9} m/cycle to 5×10^{-11} m/cycle, i.e., at a stress intensity factor very close to its threshold value.

After pre-cracking, the main crack growth rate test was carried out in a load increase mode up to a crack length of $a = 2.4$ mm. In the used resonance setup, the stress ratio is directly related to the crack length based on the energy balance [57]. During the experiment, R decreases from $R = -1$ to -1.4. Following the formulas of Newman [58], the effect of this decrease should be rather small. However, in the scope of the present paper we follow the recommendation of ASTM 647 and do not consider the negative part of the cycle by using the maximum value $K_{\max}$ and the effective range ΔK_{eff} to characterize the loading. During the test, the resonant (loading) frequency decreased from ~260 Hz to ~200 Hz. The crack length measurement was based on differential compliance, e.g., on compliance difference of a sample with an open and a closed crack. Both compliances were in-situ evaluated by fitting the vibration waveform measured by accelerometer with piecewise harmonic function derived from the model of the vibrating H assembly. The model assumes small scale yielding and uses standard shape functions [59] to relate the crack-added compliance to the crack length and the stress intensity factor. This approach eliminates the influence of the sample clamping and changes in its mechanical properties. Moreover, the compliance changes sharply at the crack opening load, enabling to estimate the effective stress intensity factor range ΔK_{eff}. This "remotely sensed" opening stress ensures that most of the crack is open; however, it does not guarantee opening of the most important part directly behind the crack tip. That said, the obtained ΔK_{eff} values need to be interpreted carefully. More detailed description of the fatigue crack growth rate test method and set-up can be found in [57]. The differential compliance method was already validated for aluminum alloy and steel in [60]. After the crack growth rate test, the samples were ruptured using static three-point bending tests to allow fractographic analysis of the crack surfaces.

2.12. Statistical analysis

For all the tests, the reported data refer to averages of minimum three independent measurements and the corresponding standard deviations. Two-tailed unpaired T-student test was used to determine the statistical significance between different series ($^{*}p < 0.05$, $^{**}p < 0.01$, $^{***}p < 0.001$).

3. Results and discussion

The presentation of results and discussion is divided in two main parts, optimization of process parameters and mechanical properties of the deposits after post heat treatments.

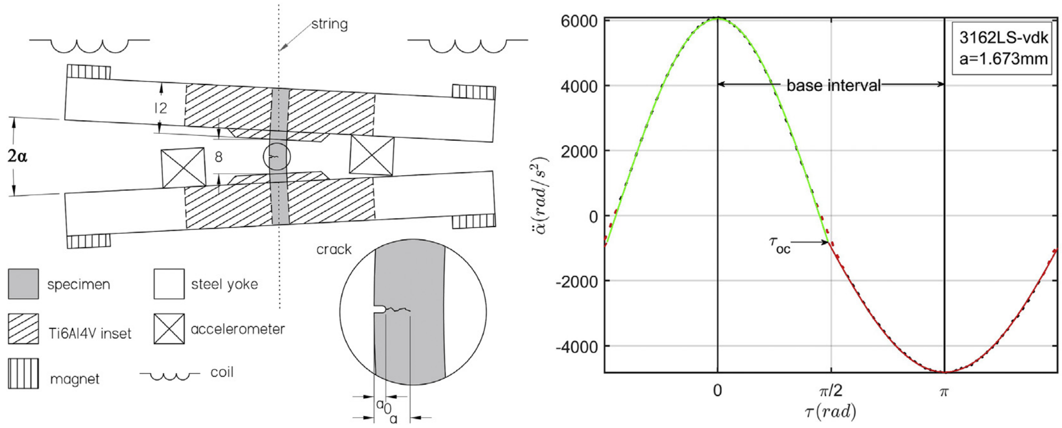

Fig. 2. Left: schematic drawing of the resonance bending fatigue crack growth test layout. Right: a typical measured (dots) and fitted (lines) vibration waveform in a phase (time) domain. Here, $\ddot{\alpha}$ is the yoke angular acceleration describing the specimen bending moment, $\tau = 2\pi t/T$ is the phase of vibration, and τ_{OC} corresponds to the crack opening.

3.1. Optimization of as-sprayed deposits

This section elucidates the strategies used in the present study to develop 316 L deposits that exceed quality thresholds for building freestanding parts and allow for further improvement by heat treatment to obtain high structural integrity. Moreover, this section explores correlations between calculated quality parameters and different properties as strength and electrical conductivity to allow for guidelines on how to experimentally tune deposit development by non-destructive on-site part testing. Respective strategies should be transferable to the development of any other material utilized in CS for AM.

3.1.1. Cold spray parameter selection

Based on the calculations using the KSS software, Fig. 3 shows the particle impact velocities and temperatures for the two different powder sizes according to the corresponding PSDs under different spray parameter sets. The critical velocities to be exceeded for successful impacts are given by solid and dashed lines for the fine and coarse powder sizes, respectively. For the spray parameters under investigation, the particle impact conditions by far exceeded the critical velocities. However, for each spray parameter set, the individual particle impact condition can significantly depend on the size. Smaller particles by their lower momentum accelerate to higher velocities as compared to the larger ones. Despite reaching high temperatures before the nozzle throat, the smaller particles impact at lower temperatures than the larger ones. This is due to the smaller thermal momentum of small particles and thus more effective cooling by the gas jet in the expanding regime of the nozzle and the free jet. For obtaining homogeneous deposit quality, spray conditions must be tuned for a similar excess of impact velocity against critical velocity. The calculations show that such is appropriately valid for the selected spray conditions. According to the calculation results, using an injection distance of 65 mm upstream nozzle throat seemed to be sufficient to pre-heat also larger particles.

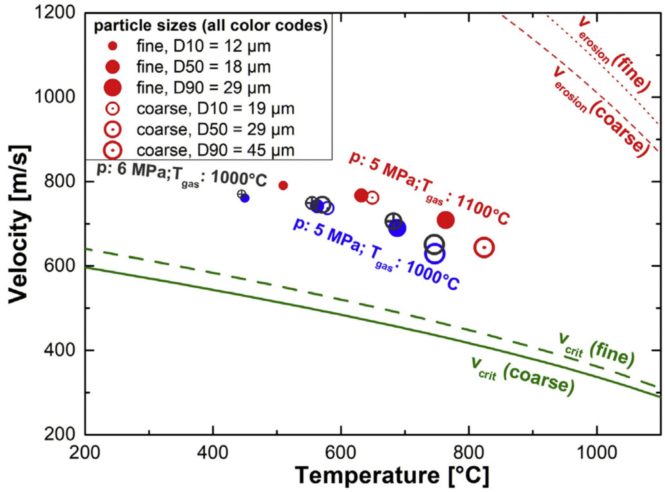

Fig. 3. Calculated particle impact conditions and critical velocities for CS of the two steel 316 L powders.

The increase of gas temperature at constant pressure of 5 MPa from 1000 °C to 1100 °C results in overall higher particle velocities and temperatures, and thus higher excess to critical conditions for bonding (Fig. 3). In contrast, at constant process gas temperature of 1000 °C rising the gas pressure from 5 to 6 MPa only slightly increased particle velocities, associated with small losses in impact temperature. Based on the calculated impact conditions, the deposits quality parameters η as a ratio between impact velocities and critical velocities are approximated, as given in Table 1. It has to be noted that the particle is exposed to the hot process gas only for less than about 5 ms. Due to cooling by the expanding gas in the diverging nozzle regime and the free jet, particle impact temperatures are significantly lower than the initial gas temperature and, depending on size and thermal history, typically range between 300 and 800 °C [61]. Due to their higher thermal momentum, larger particles retain more heat and have higher temperatures upon impact as compared to the smaller ones (Fig. S2). By their lower inertia, smaller particles are accelerated to higher velocities than bigger ones (Fig. S3). This explains why larger particles under ideal CS conditions should have lower impact velocity and higher impact temperature than smaller ones. This allows bigger particles to compensate their lack in velocity by less needed energy for causing thermal softening and adiabatic shear instabilities.

3.1.2. Experimental validation of as-sprayed properties

The numerical results were experimentally explored by applying the suggested range of parameter sets. Tensile testing and analyses of electrical conductivity were considered as measures of deposit quality for all applied parameter sets in the as-sprayed state. As given in Table 1 and Fig. 4, the tensile tests confirm that the gas temperature is the most influential parameter on the deposit quality in the as-sprayed state. Similar trends were observed in the electrical conductivities of the as-sprayed samples. The tensile strength improved by almost 26% for both powder types as the gas temperature increased, while particle size had a less significant effect on the mechanical strength of the samples within the studied range. No notable difference was observed in the tensile test data of samples extracted parallel (L) and perpendicular

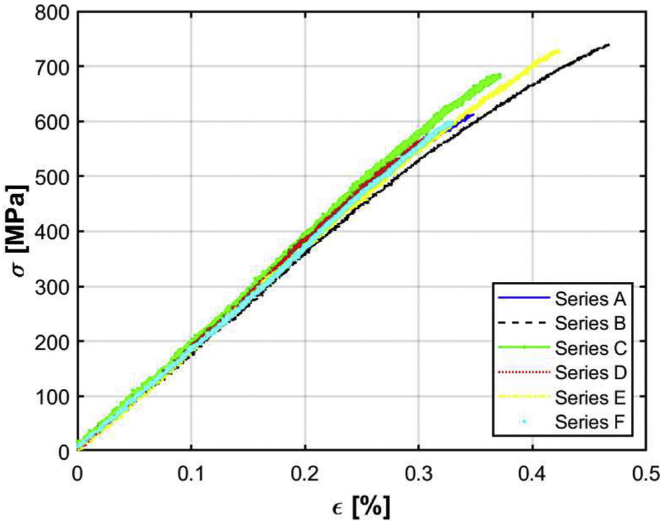

Fig. 4. Engineering stress-strain curves obtained for different sets of spray parameters series A-F (as-sprayed condition).

(T) to the movement direction of spraying nozzle (Fig. S4). This is in agreement with our past studies that confirmed the global homogeneity of the microstructure and mechanical properties in the plane of CS deposits [62]. Thus, the final samples were all taken from transverse direction, i.e., perpendicular to the torch movement direction.

Higher scatter was observed in the data for sample C as compared to the other samples. Generally speaking, the scatter could be attributed to the brittleness of these series. Using dog-bone samples with rectangular cross-sections could have made the samples susceptible to local stress concentrations at sharp corners or imperfect fillets. Bearing these deviations in mind, the optimized set of parameters was selected using a combination of tensile test data and electrical conductivity measurements, thereby trying to reduce the effect of scatter in the UTS data of some samples in the final choice.

The ultimate tensile strength (UTS) data in a range of about 600 to 760 MPa are already comparable to those of soft annealed or more than 25% work hardened bulk material [63]. The electrical conductivities reach up to 90% in comparison to soft annealed steel 316 L. Both demonstrate an exceptional good deposit quality for all used parameter sets, already ensuring close to bulk properties. Moreover, the data exhibit good correlation between the estimated η values and the measured UTS. While keeping the gas temperature and pressure constant, the data presented in Table 1 also reveal that the coarse powder tends to result in higher UTS, and slightly lower electrical conductivity as compared to samples deposited using fine powder. All measured deposit porosities are well below 1%.

3.1.3. Discussion of strategies for optimization of as-sprayed deposits

Using two different powder sizes and three spray parameter sets within a high pressure/high temperature regime, the CS process was optimized pairing modelling tools with experimental analysis. Effects of spray parameter sets on deposit qualities were evaluated on basis of electrical conductivity and mechanical strength. The correlation between the calculated quality parameter η and the deposit properties is used as verification of applied concepts and for identifying the most promising set of parameters to guarantee high deposit quality by minimizing amounts of non-bonded internal interfaces. Fig. 5 compares the development of tensile strengths and conductivities with calculated η-values and depicts the correlations between the experimental data (cf. Table 1). As shown in Fig. 5a, deposit strength increases rather linearly with η-values, in good agreement to the original concept reported by Assadi et al. [4]. Gas temperature was identified as the most essential parameter, as its increase results in higher particle velocity and promotes thermal softening of the powder particles, both of which cause more deformation and higher flattening. As shown in Table 1, keeping all the parameters constant and varying particle sizes, coarser powders result in higher η-values and thus better tensile deposit strength as compared to the finer batch. Thus, the combination of the coarse powder and the parameter sets guaranteeing best strength at an η-value of 1.59 (set B, $p_{gas} = 5$ MPa, $T_{gas} = 1100$ °C) is identified to be the optimum condition to process deposits for in-depth strength and fatigue analyses. Interestingly, the properties attained by using the fine powder are better than expected according to the η-concept. In case of the strength, this might be due to more homogenous powder microstructures with less partitioning by rapid solidification. In any case, it indicates that the deformation of the fine powders is not hindered by higher oxygen content, possibly given by its higher surface to volume ratio in comparison to coarser ones. However, the deviations between the two powders should not be over-interpreted, since the parameter variation just covered a narrow regime of high-end impact conditions. Thus, also secondary influences caused by size distribution could play a role. For instance, higher surface temperatures can increase deposit quality [12]. In the present case, it might be speculated to which extent deposits of smaller splats can restrict heat diffusion more effectively by more uniformly distributed defects that can ensure higher surface temperatures.

For the two different powder size batches, the electrical conductivities individually increase with η-values, as shown in Fig. 5b, indicating that the use of finer powders at similar η-values causes higher electron mobility in the deposit as compared to that of the coarser feedstock. A similar trend can be observed in the correlation between electrical conductivity and strength (Fig. 5c). The difference between the two powder sizes can be explained by the type of defects restricting individual properties such as strength or conductivity. While strength is mainly determined by the amount of well-bonded internal interfaces, any sort of defects, including non-bonded splats, distribution of solute atoms,

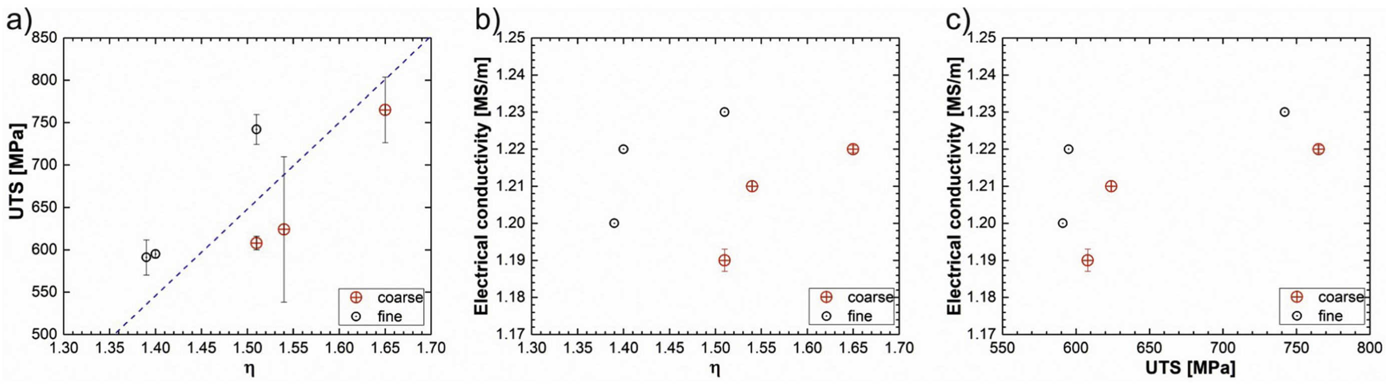

Fig. 5. Correlation of deposit properties in as sprayed state as obtained by varying the CS conditions. a) UTS versus η, b) electrical conductivity versus η, and c) conductivity versus UTS. The linear fit in a) was calculated with a R-square (COD) of 0.93. The individual square root-dependencies of the conductivities for the two powder batches do not allow for reliable fits.

internal grain boundaries or dislocation densities, can influence the electrical conductivity. Comparatively higher conductivities of the deposits formed from the smaller powder might be interpreted in terms of overall lower dislocation density. Despite above explained limits, the comparison demonstrates that for each PSD, the electrical conductivity correlates well with deposit tensile strength. Thus, conductivity analyses could be used during deposit development as a fast, low costly and non-destructive tool in serial production in comparison to tensile testing.

3.2. Influence of post treatments for improving deposit characteristics

Section 3.1 described how to obtain optimum deposit quality. However, even under optimum conditions, deposit performance can be still restricted by (i) residual amounts of non-bonded interfaces acting as crack nuclei and (ii) low plasticity due to work hardening. Both can be resolved by post deposition heat treatments. Section 3.2 explores the achievements reachable by heat treatments as isothermal annealing or HIP. With respect to load-bearing parts, major focus is given to improvements of the fatigue resistance. The comparison of annealing and HIP is provided to leave a choice for a more economical solution for final parts, if possible.

3.2.1. Tensile behavior of optimized deposits

Fig. 6 shows the stress-strain plots for the optimized set of parameters (series B) before and after heat treatments. Table 2 summarizes the mechanical properties of this series. While the yield strength of the as-sprayed samples (assumed for these samples as the stress causing a deviation from linearity equal to 0.02%) was about 64% and 98% higher than that of annealed and HIPed series, respectively, the UTS of the as-sprayed samples was about 4 to 8% higher than that of heat treated ones. The results indicate quite brittle behavior of the as-sprayed samples and a significantly higher elongation to failure with over 10-fold increase to a strain of about 50% after the heat treatments. From the inserts in Fig. 6, it can be seen that the as-sprayed samples failed at the section corresponding to the fillet radius without changing shape, while the annealed ones show notable elongation, reduced cross sectional areas, and even necking in the elongated regime, confirming the high ductility after heat treatments. The elongation to failure of the heat treated samples is rather similar to that of soft annealed bulk material. The fracture surfaces of the tensile test samples (Fig. S5) confirm the role of heat treatments in recovering ductility and pronounced dimple failure.

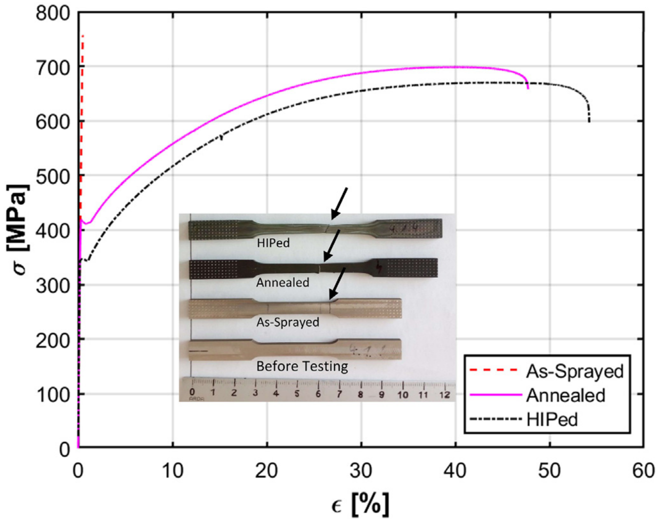

Fig. 6. Engineering stress-strain curves for samples sprayed using optimum parameters (B series) before and after heat treatments; arrows indicate the fraction section (AS: as-sprayed).

3.2.2. Deposit microstructure, porosity and microhardness

Deposits microstructures, as obtained under optimum spray parameters, are displayed in Fig. 7. Image analysis of the micrographs indicated a particle flattening ratio of 0.36 ± 0.09 that designates the high extent of deformation in the deposition process as confirmed by the greatly flattened splat shapes observed in Fig. 7a. The dispersed porosities, highlighted in the SEM images of the as-sprayed and annealed samples, are often concentrated at the interface between the splats. That might be attributed to limited deformability unable to close small gaps and to the remnants from material jets [6], with locally higher impurity or oxide contents getting removed during sample preparation. Only in rather rare cases, some large pores were observed in the cross section of the as-sprayed samples (see Fig. S6) that could be attributed to detaching of loosely bonded splats during metallographic preparation.

Both heat treated samples present a more homogeneous microstructure that barely allows to distinguish original splat boundaries. Atomic diffusion, associated recrystallization and grain growth heal out the defects present in the as-sprayed state. The examples demonstrate that the microstructure reorganization is growing over particle-particle interfaces, not being influenced by possible impurities on the original particle surfaces. This is evident by comparing the grain sizes, and the increase from the as-sprayed to the heat treated cases. Particularly, the HIPed sample shows a regular, completely recrystallized microstructure with polygonal geometries and typical 120° angles between multiple grains referring to a lower grain boundary energy configuration [68]. In addition, annealing twins dominated the microstructure due to the atomic structure reorganization during the heat treatments.

The last row in Fig. 7a-c shows the SEM micrographs in backscattering contrast mode illustrating the evolution of porosity from the as-sprayed state to the heat treated ones. The very low porosity of the as-sprayed samples confirms the efficiency of the spray parameter optimization in stage 1. Porosity results shown in Fig. 7d indicate that both heat treatments reduce the bulk porosity from about 0.8% to 0.1%. The HIP treatment resulted in a more efficient porosity decrease thanks to the increased atomic diffusion at splat interfaces activated by the high temperature accompanied by the effect of isostatic pressure.

The micro-hardness of the as-sprayed samples is higher than that of the reference bulk material [26] (see Fig. 7e). This is attributed to work hardening generated by the plastic deformation upon impact. Annealing and HIP treatments resulted in hardness reduction of about 50% and 54% with respect to as-sprayed sample, respectively.

3.2.3. Deposit crystallographic structure and microstrain

As shown in Fig. 8, the diffraction pattern of the as-sprayed, annealed and HIP treated samples reveal the FCC structure of austenitic steel 316 L (PDF# 00–033-0397). The Rietveld refinement plots of all series are shown in Fig. S7. No secondary phase precipitates were identified. The texture varied among the samples and was somewhat different to a model γ-Fe material. The as-sprayed material exhibited moderate texture (preferential orientation) that was diminished after annealing. We cannot easily assess the influence of such texture on the mechanical properties as its effect is superimposed with the overall effect of the plastic deformation experienced by the sprayed material. Peaks with increased intensity compared with model γ-Fe are indexed in the spectra (Fig. 8). A detailed mutual comparison of the spectra for the three sample types revealed significantly broader peaks in the spectrum of the as-sprayed state. As opposed to the annealed and HIPed series, this indicates a higher amount of defects being present by the deformation of the as-sprayed material. Such could be due to the smaller crystallite sizes (coherent diffraction domains, CDD) and local microstrains. The quantification of the former by Rietveld analyses provided CDD values of 59 nm for the as-sprayed and 236 nm and 253 nm for the annealed and HIPed states, respectively. The microstrain was calculated

Table 2
Mechanical properties of the CS samples as obtained under optimum parameter sets (coarse powder, $p_{gas} = 5$ MPa, $T_{gas} = 1100$ °C, $\eta = 1.59$) in as-sprayed and heat treated states in comparison to conventionally fabricated bulk materials.

	As-sprayed	Annealed	HIPed	ASM annealed AISI 316 L sheet [64,65]	Hot rolled/forged bulk material [66,67] {Kempen, 2012 #872}
Young modulus (GPa)	173.9 ± 3	190 ± 10	186 ± 12	193	–
Yield stress (MPa)	687 ± 52	418 ± 3	347 ± 0.6	290	258 ± 41
Ultimate stress (MPa)	723 ± 33	696 ± 6	672 ± 2.5	580	617 ± 35
Elongation (%)	0.47 ± 0.02	49 ± 2	53 ± 1.2	50	72 ± 9

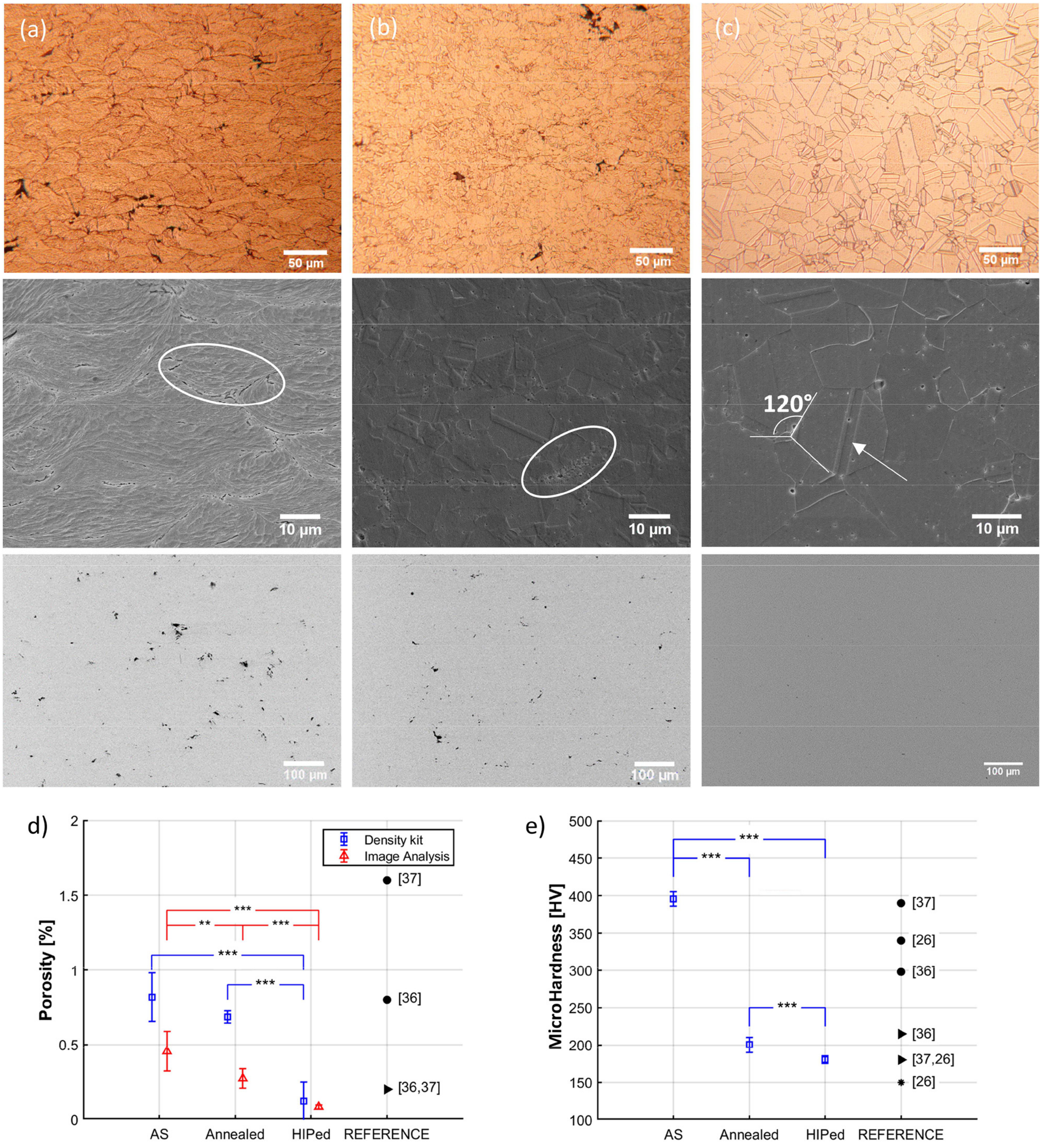

Fig. 7. Cross sectional microstructures of a) as-sprayed b) annealed and c) HIPed samples as obtained by light microscopy (top row) and SEM (middle row). Highlighted areas illustrate accumulation of pores at splat boundaries in the middle image in (a) and (b), whereas the arrow refer to twins in (c). The bottom row corresponds to the SEM micrographs in back scattering mode showing the distribution of pores; d) Porosity data obtained through image and density analysis; $N = 8$ (image analysis), $N = 4$ (density), e) microhardness data obtained on the cross section of samples (reference data in d) and e) refer to: *bulk material; ● as-sprayed and ► heat treated).

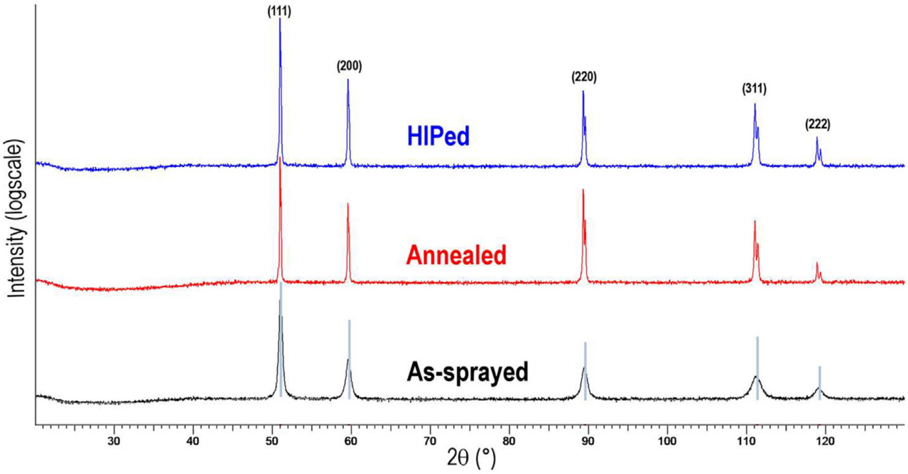

Fig. 8. X-ray diffraction spectra of the samples.

as e = 0.00104 for the as-sprayed samples, while the corresponding values for the annealed and HIPed samples were measured as non-existent. It might be stressed here that peak broadening can be affected by a variety of lattice defects, mainly dislocations or even persistent dislocation loops that survive recrystallization [69].

3.2.4. Axial fatigue strength and failure modes

Table 3 summarizes the fatigue test data, for comparison also including the fatigue strength of cast and forged bulk material, in addition to that of laser powder bed fusion (LPBF) 316 L samples [70]. The literature fatigue strength data are mainly related to a stress ratio of −1; thus, a Haigh diagram conversion was used to consider the effects of test conditions. The obtained results indicated that the fatigue strength of the CS samples corresponding to 2 million cycles is comparable to that of conventionally fabricated cast material as well as to LPBF as-built ones. Within this comparison, the annealed or HIPed samples show a slightly higher fatigue strength than the as-sprayed series.

Fig. 9 shows the fatigue fracture modes of different samples. For the as-sprayed state, the micrographs indicate a prevalent brittle behavior with limited traces of plastic deformation. The fracture surface features of the annealed samples exhibited significantly more indications of ductile failure and crack growth resistance. As compared to the as-sprayed state, the crack propagation area that was characterized by radial paths starting from the initial defects, was larger after annealing. The HIPed samples showed further improved ductility. The final rupture zone showed a predominantly plastic behavior on microscopic scale with massive presence of ductile dimples. In all cases, the cracks initiated at the surface nucleating from defects, such as residual porosities accumulated at the grain boundaries or zones of inadequate adhesion between adjacent splats. It is interesting to note that for all as-sprayed samples, the crack growth direction was parallel to the splat interfaces (along the longer Feret diameter of the splats), indicating a lower crack propagation resistance in that direction. In order to thoroughly analyze this trend, a set of fatigue crack growth tests and analysis was performed.

3.2.5. Fatigue crack growth rate

Fatigue crack growth rate $da/dN\text{-}K_{max}$ and $da/dN\text{-}\Delta K_{eff}$ curves as obtained from analyses of single edge notched samples are shown in Fig. 10 for as-sprayed and annealed samples, as well as for annealed cold rolled sheet serving as a reference. Considering the recrystallized microstructure, the HIP series was not included in the fatigue crack growth test batch. For the CS samples, two crack growth orientations were tested to address the effect of potential deposit anisotropy in the crack propagation. The cracks propagation path denoted as L-S was in the direction normal to the deposit free surface, while the L-T cracks grew in the direction parallel to the surface, as indicated in Fig. 10a. The curves given in Fig. 10b and c show ΔK_{eff} and K_{max} data. The crack growth rate curves indicate a near-threshold elbow, followed by a straight Paris region. The curves of all tested materials are similar, as are the respective threshold values. Two main exceptions indicate the anisotropy of the as-sprayed specimens: compared to other samples, the as-sprayed L-S specimens exhibit higher threshold values, and as-sprayed L-T specimens have higher crack growth rates at increased load. This anisotropy of the crack growth rates (cf. L-T and L-S curves) was not observed after the annealing, nor was it observed for the cold rolled reference materials.

The shape of the crack growth rate curves can be related to their micro-mechanism of failure. The fractographic observations (Figs. 11 and 12) include the fatigue crack growth features in the near-threshold and the high stress intensity factor zones, as well as the static rupture area formed by three-point bending after the crack growth rate test. The macrographs in Fig. 6 show a brittle behavior of the as-sprayed samples without any necking, while the annealed and HIPed samples exhibit necking. The difference between the as-sprayed and annealed sets corresponds to the improvement in the deformation properties as detected by the tensile testing. In addition, the fracture surfaces of as-sprayed samples exhibit a pattern in the fractographic features that seems to correspond to individual nozzle passes.

The fractography images in Fig. 11 characterize the fatigue failure process in the near-threshold, the high-*K*, and the static failure regions

Table 3
Axial fatigue test data (run out = 2×10^6 cycles).

	As-sprayed	Annealed	HIPed	Cast material	Forged material	LPBF material
Fatigue strength (MPa)	130 ± 6	160 ± 3	140 ± 3	144 [71] 150 [72] 154 [70] 131 [73]	190 [74] 207 [72] 226 [70] 217 [75]	87 (as built) [70] 170 (as-built turned) [70] 182 (annealed-turned) [70] 190 (HIPed-turned) [70]

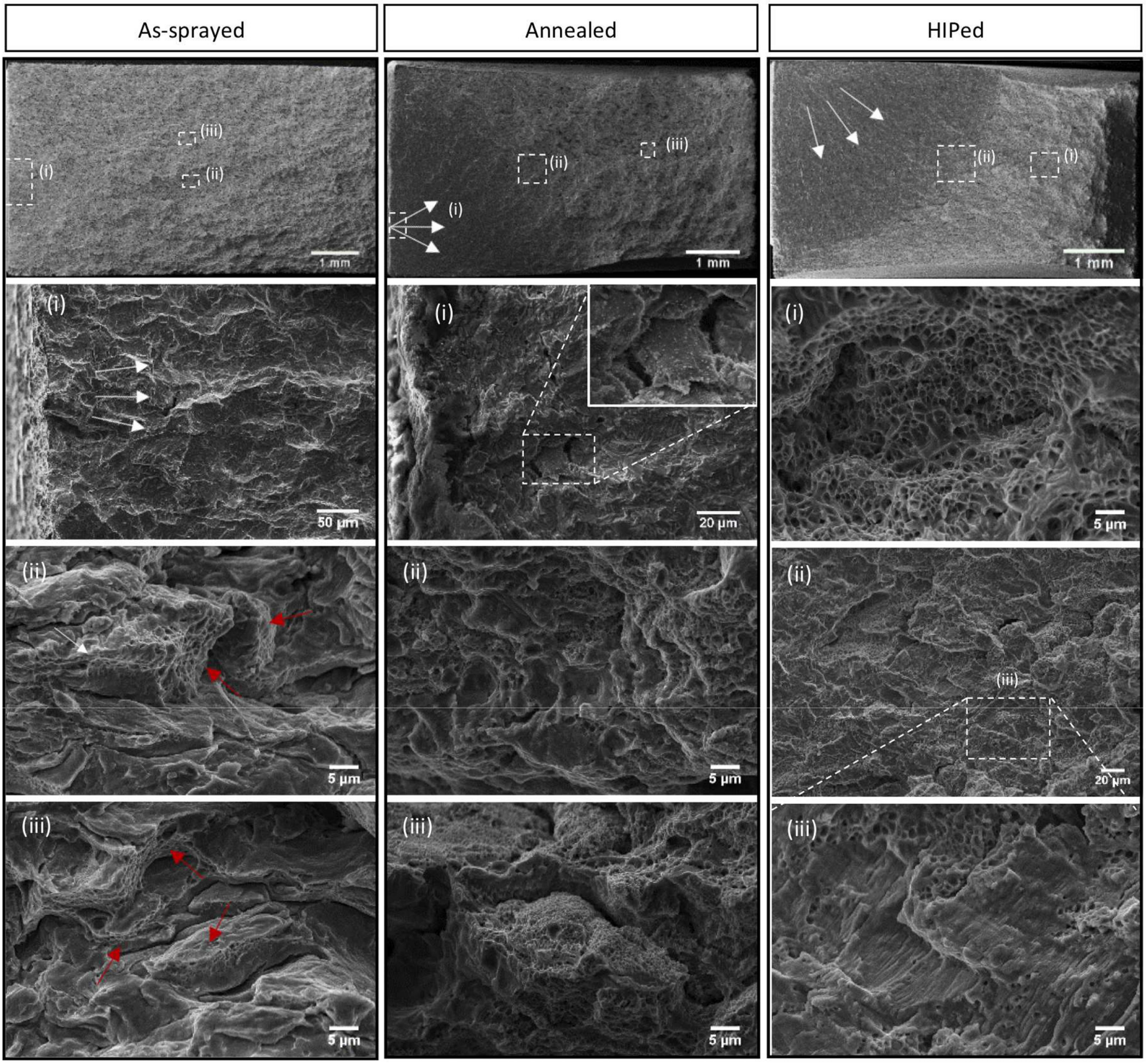

Fig. 9. Fractography analysis of as-sprayed, annealed, and HIPed fatigue test samples. For the as-sprayed sample fracture surface (i) indicates initial defects with crack propagation direction highlighted by the white arrows, and (ii) & (iii) fracture surfaces with red arrows denoting limited presence of ductile dimples. For the annealed sample, the radial crack propagation direction is highlighted by the white arrows (i). Detail of initial defects indicate (ii) crack propagation in the fracture transition area, with visible presence of dimples, and (iii) fracture areas indicating notably plastic behavior and partly presence of dimples. For the HIPed sample, (i) radial crack propagation direction is highlighted by the white arrows. (ii) shows fracture areas with apparent plastic behavior and extensive presence of dimples. Details in (iii) show the propagation in the fracture transition area indicating striations referring to a stable crack propagation.

of as-sprayed and annealed specimens. In the near-threshold region (green dots in Fig. 11), the cracks propagated mostly trans-granularly (indicated as TG). In this mode, mainly the grain size and the possible work hardening can influence the crack morphology. While in the fine-grained as-sprayed samples, the fracture surfaces of individual particles were rather planar (indicating a very fine microstructure, see as-sprayed microstructure in Fig. 7), the significantly rougher fracture of the particles in the annealed samples indicates a coarser microstructure of the material (see Fig. 7).

The similarities in appearance of as-sprayed and annealed states indicate that work hardening is playing a less prominent role with respect to crack growth in the near-threshold region. But also, in the high-*K* regions, adjacent particles influence the crack propagation in the as-sprayed L-S samples by inter-particle decohesion modes (denoted by IP in Fig. 12). Acting as a possible barrier for further crack propagation, the interfaces seem to have forced the crack to reinitiate at a slightly offset crack plane in order to propagate into the next particle. Such effects at particle interfaces are not found in the as-sprayed L-T oriented samples in the near-threshold regime. This is because the interface regions were mostly parallel to the crack growth direction.

In the high-*K* region (red dots in Fig. 11), the failure mechanisms of the as-sprayed and annealed samples differ significantly. The as-sprayed samples failed mostly by inter-particular decohesion with infrequent trans-particular fracture. Such decohesion probably

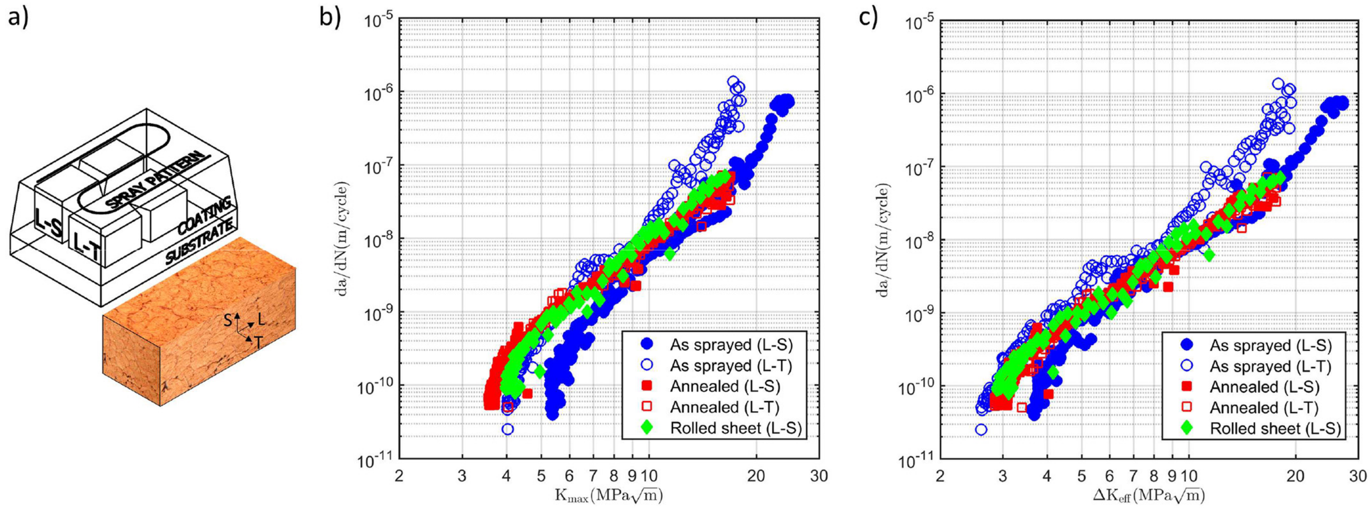

Fig. 10. Crack growth analyses with a) schematic illustration of the crack plane, crack propagation path and corresponding microstructure for the crack growth rate tests. Results for b) ΔK_{eff} and c) K_{max} of the crack growth rate tests. The stress ratio decreased from $R \sim -1$ in the near-threshold range to $R \sim -1.4$ in the high-K range. The value of ΔK_{eff} was estimated from the sample compliance change. Note the increased threshold values of as-sprayed L-S samples and an increased slope in the Paris regime of curves corresponding to as-sprayed L-T samples.

accelerated the crack growth rates and could be the cause of the higher Paris slope of the as-sprayed samples in L-T orientation in Fig. 10. The transition from the initial trans-granular (observed at near-threshold region) to this inter-particular decohesion occurs at overall crack lengths of about 1.9 mm, corresponding to a crack growth rate of about 2×10^{-8} m/cycles. The transition in the as-sprayed samples reflects the splats orientation, being stepwise in the L-S orientation, as opposed to a more gradual transition observed for the L-T orientation. In the annealed state and the reference samples, the crack in the high-*K* region propagated by striation mechanism, creating typical striation fields (SF in Fig. 12) with an occasional inter-granular fracture (IG in Fig. 12).

In the final static fracture formed by three-point bending, inter-particle decohesion can then be identified as the main failure mode of the as-sprayed samples (blue dots in Fig. 11). Only the well bonded interfaces of the particle-particle contact regions were capable of transferring the stress by causing plastic deformation as indicated by the occurrence of ductile dimples (DD in Fig. 12) and other signs of plasticity. This is in accordance with the straight, undistorted cross section of as-sprayed samples after the final static fracture shown in Fig. 6. On the other hand, the static fracture of the annealed and reference samples was dominated by ductile dimples showing also a significant geometrical distortion of the sample cross section. As a direct consequence, the fracture toughness of the as-sprayed samples could be expected to be significantly lower than that of the reference and the annealed samples, due to effects of work hardening. The fracture surface of the rolled sheet serving as reference (see Fig. S8) shows mainly trans-granular failure with striation fields dominating the high-*K* region. The static rupture of this sample was ductile, with shear dimples indicating a high degree of deformation at fracture.

3.2.6. Discussion of deposit properties after post heat treatments

For ensuring the best performance, only the parameter set for optimum properties in the as-sprayed state was selected for further investigations. Tensile tests revealed a brittle behavior for the as-sprayed samples with almost null elongation to failure, caused by the notable work hardening induced upon impact, and the presence of some non-bonded interfaces within the deposit. The high ultimate tensile strength in the as-sprayed state indicated the high deposit quality (Table 2). The sample's extraction direction (longitudinal, i.e., parallel to the spray trajectory vs. transversal, i.e., perpendicular to the spray trajectory) was found to have no significant influence on the mechanical strength of the deposits, confirming the in-plane homogeneity of the deposit global properties (Fig. S4).

The applied heat treatments restored the ductility of the deposited material, leading to elastic-plastic behavior similar to that of bulk steel 316 L. This improvement is due to diffusion causing better interparticle bonding and recrystallization restoring material ductility. Recrystallization is also the main reason for slight reduction of the UTS of heat treated samples compared to the as-sprayed ones. Previous experiments have shown that the mechanical strength of CS 316 L deposits

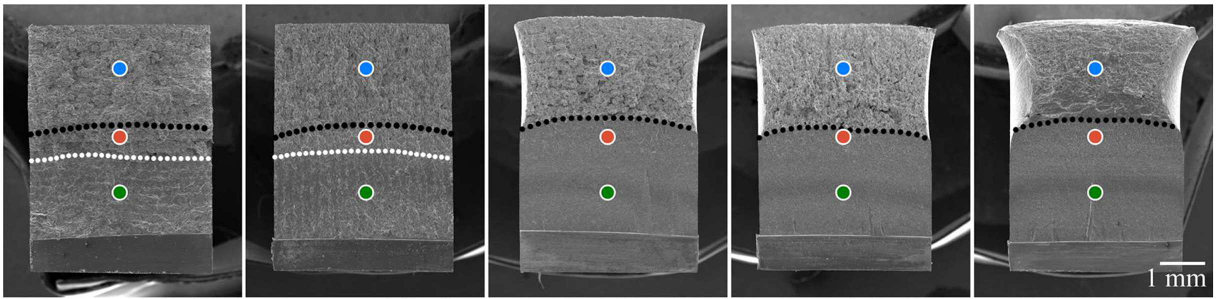

as-sprayed (L-S) as-sprayed (L-T) annealed (L-S) annealed (L-T) rolled sheet (L-S)

Fig. 11. SEM macrographs of the fracture surfaces after fatigue crack growth rate tests. The white dotted line marks the change in fracture mode from planar, trans-granular to particle decohesion-dominated regions. The black dotted line indicates the interface between the fatigue and static (three-point bend) rupture regions, clearly visible in the annealed and the reference samples. The colored dots correspond to the three areas presented in more detail in Fig. 12 (green – near-threshold, red – high-*K*, blue – static rupture).

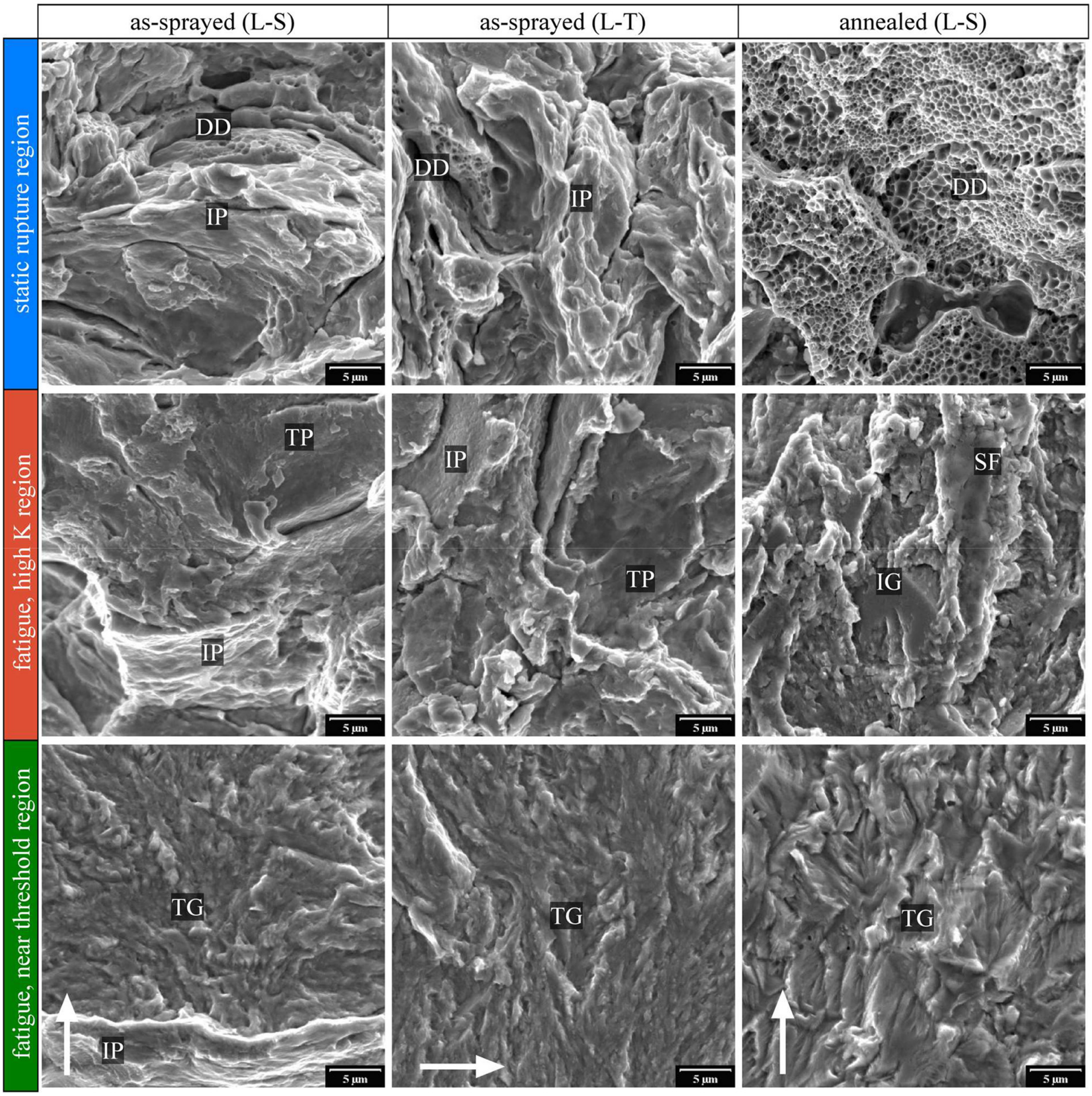

Fig. 12. SEM micrographs of fracture surfaces of fatigue crack growth rate samples in the regions of near-threshold, high-*K* and static rupture (corresponding to colored dots from Fig. 11). The white arrows indicate the crack growth direction. Nomenclature: IP – inter-particle decohesion, TP – trans-particle fracture, TG – trans-granular fracture, IG – inter-granular fracture, SF – striation field, DD – ductile dimples.

is more affected by the improved characteristics of inter-particle bonding than by the influence of reduced porosity [38]. The associated elongation to failure reaches 49% for annealed and 53% for HIPed samples. This rather ductile behavior is not only due to recrystallization, but also due to the excessive grain growth induced by HIP treatment. It is noted that the mechanical properties in all conditions here outperform previously published data on steel 316 L CS deposits [37,38]. The larger statistical scatter of the results for the as-sprayed series indicates that the heat treatments promote homogenization of the microstructure and therefore ensure more uniform mechanical properties.

Microstructural analysis of the as-sprayed samples showed highly deformed splats. The extent of the plastic deformation was evaluated by quantifying the flattening ratio. Within the resolution of OM/SEM micrographs, apart from deformation, only minor microstructural rearrangements were detected in as-sprayed samples. The microstructures show no obvious traces of thermal recrystallization. Only in the vicinity of the particle-particle interfaces smaller grain sizes are obtained, obviously due to dynamic recrystallization during the rapid deformation [69,76]. Thus, the global microstructural appearance of the as-sprayed samples indicates that the spray process did not notably change the original features of the powders. The interparticle boundaries and the resulting local porosities could be clearly distinguished in the as-sprayed samples' cross sections. In contrast, the annealed samples appear rather homogenous, showing no deformation features and less non-bonded particle-particle interfaces. This is attributed to the atomic diffusion causing recrystallization and to the high surface mobility closing the initially weakly bonded interfaces. The HIPed samples revealed a strongly homogeneous microstructure with fully recrystallized and reorganized crystalline grains. There were no traces of the original splats, and the full reorganization was confirmed by the formation of 120° angles formed between adjacent grains to reach lower grain boundary energy configurations. We postulate that the HIP parameters can be further optimized choosing a cooling rate more relevant to the sample size to restrict grain growth in the samples. As much as the HIP treatment provides slightly improved characteristics than annealing, cost-driven applications may in fact aspire for the latter method. Therefore, the final choice of post-treatment method should be based on an individual assessment of such requirements.

Both volumetric and cross sectional methods used to evaluate porosity showed significantly lower porosities obtained for the as-sprayed state with respect to the data reported in the literature [24,36–38], thanks to the optimized spray process. This indicates that N_2 can be used as a rather cheap process gas to obtain high quality 316 L deposits, under the prerequisite that spray parameters are tuned for high particle velocities and temperatures meeting η-values >1,5. The post-heat treatments resulted in a further porosity reduction caused by atomic diffusion at interparticle interfaces. Particularly, the combined effect of high temperature and pressure in HIP promoted additional material flow and thus better pore closure than annealing.

The low scatter of the microhardness measurements indicated quite homogeneous distribution across the sample volumes. Both heat treatments noticeably reduced the deposits' microhardness, with the lowest values measured for the HIPed samples; this could be attributed to the full recrystallization and much larger grain size as compared to the other conditions. In comparison to the data available in the literature [36,37], the higher microhardness obtained here is most probably due to the larger amount of work hardening induced by spraying under the optimized spray parameters, and most probably lower deposit porosity.

Crystallographic analysis indicated no phase alteration either upon deposition or after the heat treatments, as all samples contained only the FCC γ-phase typical for austenitic iron-based steel. The stability of the γ-phase is due to the 10–14% nickel content, which maintains the austenite perfectly stable up to temperatures of around 1400 °C. Broader peaks identified for the as-sprayed samples indicated high degrees of deformation due to microstrain and smaller crystallite sizes; both of which diminish after the heat treatments due to sufficient dislocation motion and diffusion.

Only for the freestanding as-sprayed samples, high compressive residual stresses were detected close to the surface (up to a depth of 0.05 mm) caused by the machining effects (Fig. S9a). Negligible residual stresses were measured for the original deposits (i.e., before machining and detachment from the substrate); this observation confirmed that the high process gas temperature together with local heating upon plastic deformation could lead to relaxation of the residual stresses caused by the peening effect of the subsequent impinging particles [77,78]. The residual stress measurements after the annealing and HIP treatments confirmed the ability of these treatments to release the residual stresses induced upon deposition and EDM cutting process.

The axial fatigue tests were aimed to gain information on the lifetime of freestanding parts. The results revealed fatigue strengths similar to the literature data for cast and LPBF bulk material [70–73]. The final fracture surface of the as-sprayed samples represented prevalent brittle behavior with limited traces of plastic deformation. Mixed mechanism of inter-particle (rounded shapes typical for a complete splat detachment) and intra-splat fracture (cleavage planes) was observed; only small areas showing ductile dimples, representing the quite limited ductility. Annealing and HIP treatments improved the fatigue performance. After annealing, the fatigue strength exhibited an increase of around 20%, thanks to the ductility restoration. This improvement is attributed to a better inter-particle bonding provided by atomic diffusion at the splats' interfaces, as well as porosity reduction. The fracture surfaces of annealed samples showed a strong plastic behavior on a microscopic scale with the presence of diffused and consistent dimples. HIPed samples, on the other hand, showed slightly lower fatigue strength than the annealed ones. This can be partly attributed to the significant grain growth and lower tensile strength of these samples. The fracture surface of HIPed series to a large extent exhibited traces of plastic deformation. It is to be noted that the samples' surface roughness (Fig. S10) is rather low after the milling steps (R_a of 0.67 μm) and comparable for the different treatments.

From the crack growth rate analysis and corresponding SEM observation of the fracture surfaces, it emerges that inter-particle contact regions played the most important role in defining the fracture micro-mechanisms in both static and fatigue failure modes of the as-sprayed samples. These interface regions are characterized by excessive work hardening and a limited localized particle cohesion [28]. Acting as crack propagation barriers, the interfaces contributed to the observed anisotropy in the crack growth rate behavior for the as-sprayed condition when they were preferably oriented perpendicularly/parallel to the crack propagation direction. The cracks propagating along the deposit buildup direction (L-S) faced the interface regions in a perpendicular direction and growth was slowed down significantly. In contrast, the cracks growing perpendicular to the buildup direction (L-T) propagated along the flattened splat interfaces with no significant retardation. This barrier effect may have caused the increased threshold value of the as-sprayed L-S samples. In the high-*K* region, as confirmed by fractography images, the existence of interface regions led to particle decohesion. Such whole splat detachment mode increased the crack growth rates of L-T oriented as-sprayed samples, reaching values significantly higher than those achieved by the striation mechanism observed in the annealed conditions and the L-S as-sprayed specimens. The particle decohesion at splat interfaces was also identified as the reason for brittle static behavior. All four discussed effects of the interface regions, i.e., near-threshold crack retardation, high-*K* crack growth rate increase, crack growth rate anisotropy, and brittle static fracture were effectively suppressed by annealing. A significant increase of sample ductility was observed after annealing; thus, an increase of the fracture toughness may also be expected. The results demonstrate that CS deposits after post treatments show the same performance and failure features as conventional work hardened and heat treated bulk 316 L steel. It might be noted here that similar post treatments are needed for conventional AM techniques.

4. Summary and conclusions

This study presents a comprehensive analysis of freestanding steel 316 L deposits to evaluate cold spray as an additive manufacturing technique for the fabrication of load-bearing parts by using N_2 as process gas, making the process suitable for serial manufacturing. The results of this study provide the strategy to develop high quality load-bearing freestanding 316 L deposits by (i) optimization of the spray conditions and (ii) inside views on influence of post heat treatments. With respect to high deposition rates and low costs as compared to conventional AM techniques, the cold spray process route emerges as a competitive AM technique.

- Cold spray parameters were successfully tuned by pairing modelling tools and the experimental verification of tensile strength and electrical conductivity. The deposit properties correlate well with respective particle impact velocity to critical velocity ratios (η) in the considered high-end regime of about 1.40 to 1.65. Cold spray deposition using the optimized parameter set resulted in a homogeneous microstructure with less than 1% porosity, and deposit static strengths similar to those of respective bulk material. Conditions for reaching best deposit performance were selected for further post-processing.
- Considering the significant work hardening induced by extensive plastic deformation of powder particles upon impact and associated high hardness and brittle deposit behavior, the application of optimal heat treatments was remarkably efficient to restore ductility through promoting recrystallization and improving interparticle

bonding. Moreover, heat treatments reduced the remaining porosity, improved microstructure homogeneity and released residual stresses.

- Fatigue test data indicated outstanding room temperature axial fatigue strength corresponding to two million cycles for cold sprayed samples in the as-sprayed and heat treated configurations, that was found to be comparable to that of cast bulk material.
- Both heat treatments enhanced fatigue performance; the slightly lower fatigue data obtained after HIP could be addressed to the low cooling rate of the process resulting in excessive recrystallization and grain growth. Based on the results, standard annealing appears as a more suitable and more economical post treatment.
- The as-sprayed samples exhibited anisotropic crack growth behavior and deviated from the baseline defined by a reference cold-rolled sheet. This deviation can be attributed to planar defects at inter-particle contact areas and was efficiently removed by annealing. The annealed samples showed isotropic crack growth behavior with rates identical to that of the reference cold rolled sheet samples.

The obtained results highlight the notable mechanical strength, under static and cyclic loading, of freestanding cold sprayed 316 L deposits to be used as load-bearing components. The results enlighten the high potential of cold spray additive manufacturing as a competitive technique to overcome some of the shortcomings of the commonly used additive manufacturing routes comprising high working temperature, product size limitations and low deposition rates.

Data availability statement

The raw/processed data required to reproduce these findings can be shared upon request.

Declaration of Competing Interest

The authors declare that they have no known competing financial interests or personal relationships that could have appeared to influence the work reported in this paper.

Acknowledgements

Valuable support and input of Ing. Kai-Uwe Volker (HIP PM Volker) regarding HIP treatment is gratefully appreciated. The authors also thank Marion Kollmeier form HSU for performing the conductivity tests. The crack growth rate testing was supported by ERDF project Centre of Advanced Applied Sciences (No. CZ.02.1.01/0.0/0.0/16_019/0000778).

Appendix A. Supplementary data

Supplementary data to this article can be found online at https://doi.org/10.1016/j.matdes.2021.109575.

References

[1] V. Champagne, D. Helfritch, The unique abilities of cold spray deposition, Int. Mater. Rev. 61 (2016) 437–455.
[2] R.N. Raoelison, Y. Xie, T. Sapanathan, M.P. Planche, R. Kromer, S. Costil, et al., Cold gas dynamic spray technology: a comprehensive review of processing conditions for various technological developments till to date, Additive Manufacturing. 19 (2018) 134–159.
[3] R. Ghelichi, M. Guagliano, Coating by the cold spray process: a state of the art, Frattura ed Integrità Strutturale. 3 (2009) 30–44.
[4] H. Assadi, H. Kreye, F. Gärtner, T. Klassen, Cold spraying – a materials perspective, Acta Mater. 116 (2016) 382–407.
[5] D. Gilmore, R. Dykhuizen, R. Neiser, M. Smith, T. Roemer, Particle velocity and deposition efficiency in the cold spray process, J. Therm. Spray Technol. 8 (1999) 576–582.
[6] H. Assadi, F. Gärtner, T. Stoltenhoff, H. Kreye, Bonding mechanism in cold gas spraying, Acta Mater. 51 (2003) 4379–4394.
[7] A. Sova, S. Grigoriev, A. Okunkova, I. Smurov, Potential of cold gas dynamic spray as additive manufacturing technology, Int. J. Adv. Manuf. Technol. 69 (2013) 2269–2278.
[8] F. Gaertner, T. Schmidt, H. Kreye, Present status and future prospects of cold spraying, Materials science forum: Trans Tech Publ (2007) 433–436.
[9] W. Li, K. Yang, S. Yin, X. Yang, Y. Xu, R. Lupoi, Solid-state additive manufacturing and repairing by cold spraying: a review, Journal of Materials Science & Technology. 34 (2018) 440–457.
[10] S. Bagherifard, A.H. Astaraee, M. Locati, A. Nawaz, S. Monti, J. Kondas, et al., Design and analysis of additive manufactured bimodal structures obtained by cold spray deposition, Additive Manufacturing. 101131 (2020).
[11] S. Bagherifard, S. Monti, M.V. Zuccoli, M. Riccio, J. Kondás, M. Guagliano, Cold spray deposition for additive manufacturing of freeform structural components compared to selective laser melting, Mater. Sci. Eng. A 721 (2018) 339–350.
[12] Z. Arabgol, M.V. Vidaller, H. Assadi, F. Gärtner, T. Klassen, Influence of thermal properties and temperature of substrate on the quality of cold-sprayed deposits, Acta Mater. 127 (2017) 287–301.
[13] Y.-Y. Wang, Y. Liu, G.-J. Yang, J.-J. Feng, K. Kusumoto, Effect of microstructure on the electrical properties of nano-structured TiN coatings deposited by vacuum cold spray, J. Therm. Spray Technol. 19 (2010) 1231–1237.
[14] L. Rickenbacher, A. Spierings, K. Wegener, An integrated cost-model for selective laser melting (SLM), Rapid Prototyp. J. 19 (3) (2013) 208–214.
[15] H. Piili, A. Happonen, T. Väistö, V. Venkataramanan, J. Partanen, A. Salminen, Cost estimation of laser additive manufacturing of stainless steel, Phys. Procedia 78 (2015) 388–396.
[16] K. Spencer, M.-X. Zhang, Optimisation of stainless steel cold spray coatings using mixed particle size distributions, Surf. Coat. Technol. 205 (2011) 5135–5140.
[17] L. Brewer, J. Schiel, E. Menon, D. Woo, The connections between powder variability and coating microstructures for cold spray deposition of austenitic stainless steel, Surf. Coat. Technol. 334 (2018) 50–60.
[18] K. Spencer, D. Fabijanic, M.-X. Zhang, The influence of Al2O3 reinforcement on the properties of stainless steel cold spray coatings, Surf. Coat. Technol. 206 (2012) 3275–3282.
[19] A.-M. Bandar, R. Mongrain, E. Irissou, S. Yue, Improving the strength and corrosion resistance of 316L stainless steel for biomedical applications using cold spray, Surf. Coat. Technol. 216 (2013) 297–307.
[20] Y. Xie, M.-P. Planche, R. Raoelison, X. Suo, P. Hervé, Effect of substrate preheating on adhesive strength of SS 316L cold spray coatings, J. Therm. Spray Technol. 25 (2016) 123–130.
[21] J. Huang, W. Ma, Y. Xie, H. Fukanum, K. Zhang, G. Wang, et al., Influence of cold gas spray processing conditions on the properties of 316L stainless steel coatings, Surf. Eng. 35 (2019) 784–791.
[22] H. Fukanuma, N. Ohno, B. Sun, R. Huang, In-flight particle velocity measurements with DPV-2000 in cold spray, Surf. Coat. Technol. 201 (2006) 1935–1941.
[23] M. Villa, S. Dosta, J.M. Guilemany, Optimization of 316L stainless steel coatings on light alloys using cold gas spray, Surf. Coat. Technol. 235 (2013) 220–225.
[24] R. Cortés, M. Garrido, A. Rico, C. Múnez, P. Poza, A. Martos, et al., Effect of processing conditions on the mechanical performance of stainless steel cold sprayed coatings, Surf. Coat. Technol. 125874 (2020).
[25] B. Dikici, H. Yilmazer, I. Ozdemir, M. Isik, The effect of post-heat treatment on microstructure of 316L cold-sprayed coatings and their corrosion performance, J. Therm. Spray Technol. 25 (2016) 704–714.
[26] A. Sova, S. Grigoriev, A. Okunkova, I. Smurov, Cold spray deposition of 316L stainless steel coatings on aluminium surface with following laser post-treatment, Surf. Coat. Technol. 235 (2013) 283–289.
[27] T. Schmidt, F. Gärtner, H. Assadi, H. Kreye, Development of a generalized parameter window for cold spray deposition, Acta Mater. 54 (2006) 729–742.
[28] T. Schmidt, H. Assadi, F. Gärtner, H. Richter, T. Stoltenhoff, H. Kreye, et al., From particle acceleration to impact and bonding in cold spraying, J. Therm. Spray Technol. 18 (2009) 794.
[29] H. Assadi, T. Schmidt, H. Richter, J.O. Kliemann, K. Binder, F. Gärtner, et al., On parameter selection in cold spraying, J. Therm. Spray Technol. 20 (2011) 1161–1176.
[30] http://kinetic-spray-solutions.com/ (2018).
[31] H. Assadi, I. Irkhin, H. Gutzmann, F. Gärtner, M. Schulze, M. Villa Vidaller, et al., Determination of plastic constitutive properties of microparticles through single particle compression, Adv. Powder Technol. 26 (2015) 1544–1554.
[32] H. Assadi, F. Gärtner, Particle compression test: a key step towards tailoring of feedstock powder for cold spraying, Coatings. 10 (2020) 458.
[33] T. Stoltenhoff, C. Borchers, F. Gärtner, H. Kreye, Microstructures and key properties of cold-sprayed and thermally sprayed copper coatings, Surf. Coat. Technol. 200 (2006) 4947–4960.
[34] F. Gärtner, T. Stoltenhoff, J. Voyer, H. Kreye, S. Riekehr, M. Kocak, Mechanical properties of cold-sprayed and thermally sprayed copper coatings, Surf. Coat. Technol. 200 (2006) 6770–6782.
[35] B. Dikici, M. Topuz, Production of annealed cold-sprayed 316L stainless steel coatings for biomedical applications and their in-vitro corrosion response, Protection of Metals and Physical Chemistry of Surfaces. 54 (2018) 333–339.
[36] G. Sundararajan, P.S. Phani, A. Jyothirmayi, R.C. Gundakaram, The influence of heat treatment on the microstructural, mechanical and corrosion behaviour of cold sprayed SS 316L coatings, J. Mater. Sci. 44 (2009) 2320–2326.
[37] A.-M. Bandar, P. Vo, R. Mongrain, E. Irissou, S. Yue, Effect of heat treatment on the microstructure and mechanical properties of stainless steel 316L coatings produced by cold spray for biomedical applications, J. Therm. Spray Technol. 23 (2014) 641–652.

[38] S. Yin, J. Cizek, X. Yan, R. Lupoi, Annealing strategies for enhancing mechanical properties of additively manufactured 316L stainless steel deposited by cold spray, Surf. Coat. Technol. 370 (2019) 353–361.
[39] A.P. Iliopoulos, R. Jones, J.G. Michopoulos, N. Phan, C. Rans, Further studies into crack growth in additively manufactured materials, Materials. 13 (2020) 2223.
[40] S. Bagherifard, M. Guagliano, Fatigue performance of cold spray deposits: coating, repair and additive manufacturing cases, Int. J. Fatigue 139 (2020) 105744.
[41] B. Al-Mangour, R. Dallala, F. Zhim, R. Mongrain, S. Yue, Fatigue behavior of annealed cold-sprayed 316L stainless steel coating for biomedical applications, Mater. Lett. 91 (2013) 352–355.
[42] A.G. Gavras, D.A. Lados, V.K. Champagne, R.J. Warren, Effects of processing on microstructure evolution and fatigue crack growth mechanisms in cold-spray 6061 aluminum alloy, Int. J. Fatigue 110 (2018) 49–62.
[43] A.G. Gavras, D.A. Lados, V.K. Champagne, R.J. Warren, D. Singh, Small fatigue crack growth mechanisms and interfacial stability in cold-spray 6061 aluminum alloys and coatings, Metall. Mater. Trans. A 49 (2018) 6509–6520.
[44] O. Kovarik, J. Siegl, J. Cizek, T. Chraska, J. Kondas, Fracture toughness of cold sprayed pure metals, J. Therm. Spray Technol. 29 (2020) 147–157.
[45] R. Trivedi, W. Kurz, Dendritic growth, Int. Mater. Rev. 39 (1994) 49–74.
[46] K.-R. Ernst, J. Braeutigam, F. Gaertner, T. Klassen, Effect of substrate temperature on cold-gas-sprayed coatings on ceramic substrates, J. Therm. Spray Technol. 22 (2013) 422–432.
[47] ASTME1004, Standard Test Method for Determining Electrical Conductivity Using the Electromagnetic (Eddy Current) Method, 2017.
[48] A.A. Tiamiyu, C.A. Schuh, Particle flattening during cold spray: mechanistic regimes revealed by single particle impact tests, Surf. Coat. Technol. 403 (2020) 126386.
[49] C.A. Schneider, W.S. Rasband, K.W. Eliceiri, NIH image to ImageJ: 25 years of image analysis, Nat. Methods 9 (2012) 671–675.
[50] D. Asquith, A. Yerokhin, J. Yates, A. Matthews, Effect of combined shot-peening and PEO treatment on fatigue life of 2024 Al alloy, Thin Solid Films 515 (2006) 1187–1191.
[51] H. Rietveld, Line profiles of neutron powder-diffraction peaks for structure refinement, Acta Crystallogr. 22 (1967) 151–152.
[52] R. Hill, C. Howard, Quantitative phase analysis from neutron powder diffraction data using the Rietveld method, J. Appl. Crystallogr. 20 (1987) 467–474.
[53] R.W. Cheary, A. Coelho, A fundamental parameters approach to X-ray line-profile fitting, J. Appl. Crystallogr. 25 (1992) 109–121.
[54] W. Dollase, Correction of intensities for preferred orientation in powder diffractometry: application of the march model, J. Appl. Crystallogr. 19 (1986) 267–272.
[55] W-fj Dixon, F.J. Massey Jr., Introduction to Statistical Analysis, McCraw-Hill Book Company. Inc, New York, 1957.
[56] D. Rozumek, Z. Marciniak, Fatigue crack growth in AlCu4Mg1 under nonproportional bending-with-torsion loading, Mater. Sci. 46 (2011) 685–694.
[57] O. Kovarik, A. Materna, J. Siegl, J. Cizek, J. Klecka, Fatigue crack growth in plasma-sprayed refractory materials, J. Therm. Spray Technol. 28 (2019) 87–97.
[58] J. Newman Jr., A Crack Opening Stress Equation for Fatigue Crack Growth, 1984.
[59] T. Fett, Stress intensity factors-t-stresses-weight functions, 2008.
[60] O. Kovarik, A. Janca, J. Siegl, Fatigue crack growth rate in miniature specimens using resonance, Int. J. Fatigue 102 (2017) 252–260.
[61] C.M. Kay, J. Karthikeyan, High Pressure Cold Spray: Principles and Applications: Asm International, 2016.
[62] S. Bagherifard, G. Roscioli, M.V. Zuccoli, M. Hadi, G. D'Elia, A.G. Demir, et al., Cold spray deposition of freestanding Inconel samples and comparative analysis with selective laser melting, J. Therm. Spray Technol. 26 (2017) 1517–1526.
[63] H. Atkinson, S. Davies, Fundamental aspects of hot isostatic pressing: an overview, Metall. Mater. Trans. A 31 (2000) 2981–3000.
[64] D. Peckner, I.M. Bernstein, D. Peckner, Handbook of Stainless Steels, McGraw-Hill, New York, 1977.
[65] A.I.H. Committee, S.R. Lampman, ASM Handbook: Fatigue and Fracture/Steven R. Lampman, Technical Ed, ASM International, 1996.
[66] A.J. Cooper, W.J. Brayshaw, A.H. Sherry, Tensile fracture behavior of 316L austenitic stainless steel manufactured by hot Isostatic pressing, Metall. Mater. Trans. A 49 (2018) 1579–1591.
[67] R. Blandford, D. Morton, S. Snow, T. Rahl, Tensile stress-strain results for 304L and 316L stainless steel plate at temperature, ASME 2007 Pressure Vessels and Piping Conference, American Society of Mechanical Engineers 2007, pp. 617–628.
[68] F.J. Humphreys, M. Hatherly, Recrystallization and Related Annealing Phenomena, Elsevier, 2012.
[69] C. Borchers, T. Schmidt, F. Gärtner, H. Kreye, High strain rate deformation microstructures of stainless steel 316L by cold spraying and explosive powder compaction, Appl. Phys. A Mater. Sci. Process. 90 (2008) 517–526.
[70] K. Solberg, S. Guan, S.M.J. Razavi, T. Welo, K.C. Chan, F. Berto, Fatigue of additively manufactured 316L stainless steel: The influence of porosity and surface roughness, Fatigue Fract. Eng. Mater. Struct. 42 (2019) 2043–2052, https://doi.org/10.1111/ffe.13077.
[71] H. Ueno, K. Kakihata, Y. Kaneko, S. Hashimoto, A. Vinogradov, Enhanced fatigue properties of nanostructured austenitic SUS 316L stainless steel, Acta Mater. 59 (2011) 7060–7069.
[72] S. Teoh, Fatigue of biomaterials: a review, Int. J. Fatigue 22 (2000) 825–837.
[73] D. Paquet, J. Lanteigne, M. Bernard, C. Baillargeon, Characterizing the effect of residual stresses on high cycle fatigue (HCF) with induction heating treated stainless steel specimens, Int. J. Fatigue 59 (2014) 90–101.
[74] T. Roland, D. Retraint, K. Lu, J. Lu, Fatigue life improvement through surface nanostructuring of stainless steel by means of surface mechanical attrition treatment, Scr. Mater. 54 (2006) 1949–1954.
[75] E. Puchi-Cabrera, F. Matınez, I. Herrera, J. Berrıos, S. Dixit, D. Bhat, On the fatigue behavior of an AISI 316L stainless steel coated with a PVD TiN deposit, Surf. Coat. Technol. 182 (2004) 276–286.
[76] C. Borchers, F. Gärtner, T. Stoltenhoff, H. Kreye, Microstructural bonding features of cold sprayed face centered cubic metals, J. Appl. Phys. 96 (2004) 4288–4292.
[77] R. Ghelichi, S. Bagherifard, D. MacDonald, I. Fernandez-Pariente, B. Jodoin, M. Guagliano, Experimental and numerical study of residual stress evolution in cold spray coating, Appl. Surf. Sci. 288 (2014) 26–33.
[78] T. Suhonen, T. Varis, S. Dosta, M. Torrell, J.M. Guilemany, Residual stress development in cold sprayed Al, Cu and Ti coatings. Acta Materialia. 61 (2013) 6329–6337.